

COMPARISON OF METHODS FOR THE DETERMINATION OF TESLA TURBINE PERFORMANCE

KRZYSZTOF RUSIN, WŁODZIMIERZ WRÓBLEWSKI, MICHAŁ STROZIK

Silesian University of Technology, Gliwice, Poland

e-mail: krzysztof.rusin@polsl.pl

A numerical and experimental investigation of the Tesla turbine is presented in the paper. The experiment is conducted for various inlet pressure and load. The roughness of the rotor disc is determined as it is a key factor to obtain high turbine efficiency and power. The numerical investigations are performed for the same conditions as in the experiment. The computational results are compared with the analytical model. Comparison of performance characteristics show a relatively good agreement between the experiment and CFD. The analytical model overestimates distributions of pressure and circumferential velocities, although the predicted power is on the similar level as in the experiment and CFD.

Keywords: Tesla turbine, roughness, radial turbine

1. Introduction

Processes in a lot of types of plants are connected with waste in a gaseous form. Those waste gasses are characterised by thermodynamic parameters higher than ambient ones, which opens the possibility of reusing them in order to recuperate a small amount of energy. Such systems should be on one hand relatively cheap for sake of economic feasibility but, on the other hand, reliable. The most important part in the waste energy recuperation system, which has the biggest impact on those features, is the expander. Tesla turbine seems to fulfil the most important requirements for this purpose.

Tesla turbine is a radial turbine invented in 1906 by Nikola Tesla and patented in 1913 (Tesla, 1913). The most characteristic feature of this turbine is the rotor which consists of parallel discs coupled on a shaft close to each other. Another important component is the supply system. Its aim is to accelerate the working medium and to deliver it at an optimal angle (Neckel and Godinho, 2015). The principle of operation is based on viscosity of the fluid and adhesive forces between the disc surface and fluid particles. The working medium flows tangentially into the rotor at the outer radius and is subjected to multiple forces: inertial, centrifugal, viscous and Coriolis (Guha and Sengupta, 2013). Shear stresses coming from fluid viscosity and from flow turbulence generate the torque, which makes the discs rotate. The turbine has some unique advantages which are often missing in blade expanders (Sengupta and Guha, 2012). The turbine is resistant to erosion due to tangential flow. This feature gives bigger flexibility in selection of the working medium, which could be a multi-phase fluid or fluid contaminated with solid particles (Lampart and Jędrzejewski, 2011). These features make it possible to apply Tesla turbine in systems powered by renewable energy sources, e.g. with the low boiling medium (Lampart *et al.*, 2009). There is also a potential for use in compressed air energy storage systems (Szablowski *et al.*, 2017) or in big scale heat pumps, e.g. in CO₂ capture installations (Bochon and Chmielniak, 2015). A simple construction of turbine components increases economic feasibility of systems with this expander. The main weakness of the turbine is low efficiency. The main source of losses is the supply system. Phenomena like shock waves, overexpansion or overcompression are responsible

for nozzle efficiency drop and, therefore, worse turbine performance. Higher pressure ratios also require appropriate sealing system (Wróblewski *et al.*, 2018; Frączek *et al.*, 2017) in order to prevent leakage. Losses in the outlet system are also significantly decreasing the overall turbine efficiency and are influenced by rotational speed (Li *et al.*, 2017). The shock wave structures may also be responsible for sudden efficiency and power drop in higher rotational velocities (Song *et al.*, 2018).

In the recent years, Tesla turbine has been often a subject of research. Barbarelli (2018) tested a Tesla turbine with superheated steam at maximum temperature 200°C, and the obtained efficiency was at the level of 30%. Shock losses in the deflector, as well as in the phase change, may influence turbine efficiency in that case (Dykas *et al.*, 2015). Carey (2010) proposed a method of efficiency determination, which assumes non-viscous and incompressible flow in which the body force represents the wall shear effects. According to this model, the overall turbine isentropic efficiency within the range of 80-90% is feasible. Schosser *et al.* (2016) measured tangential and radial velocity profiles in the inter-disc gaps by means of the 3D-PTV method. Borate and Misal (2012) analysed the influence of disc spacing and surface roughness on power performance. They concluded that efficiency can be improved at least by up to 45% for optimal values of disc roughness and inter-disc gaps. Deng *et al.* (2013) developed a complex analytical model which made it possible to predict turbine performance. Moreover, 6 parameters crucial for turbine operation were determined: inlet pressure, inlet velocity, inlet temperature, disc tip Mach number, Reynolds number and radius of the rotor. Guha and Sengupta (2013) developed an analytical model which took into account centrifugal, inertial, Coriolis and viscous forces. Moreover, they proved that the turbine could work even with a negative relative fluid tangential velocity.

Preliminary experimental investigation of Tesla turbine and comparison of performance with the prediction of numerical analysis is presented in the paper. The object of interest was micro-scale Tesla turbine prototype available on the market. The research concerned the influence of inlet pressure and disc roughness on performance characteristics of Tesla turbine. The obtained results were also validated by the use of the analytical model proposed by Guha and Sengupta (2013).

2. Experimental test stand

The main aim of experimental investigations was to obtain performance characteristics of Tesla turbine. Test stand which is presented in Fig. 1 was divided into two parts: (a) supply system and (b) measurement system.

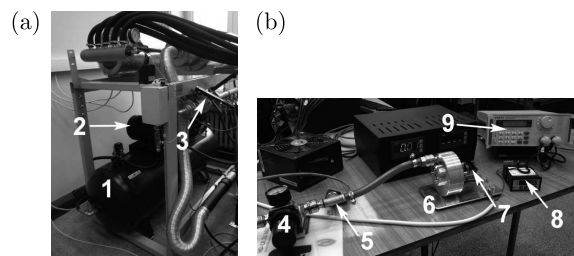


Fig. 1. Test stand: (a) supply system and (b) measurement system; 1 – air tank, 2 – compressor, 3 – main valve, 4 – membrane control valve, 5 – pressure transducer, 6 – Tesla turbine, 7 – generator, 8 – tachometer, 9 – electric load

The air tank of 0.5 m³ volume was filled up to pressure 8 bar by the reciprocating compressor. The aim of two valves was to control the mass flow rate and to precisely set appropriate pressure value, which was measured by the transducer. This value was considered as the inlet pressure

to the turbine on the assumption of no losses in the duct between the pressure transducer and the turbine. The turbine was connected to the generator, which was a brushless motor. It was connected to tachometer (8), which measured rotational velocity of the generator and turbine by analysing the frequency of the electric current. The electric load was responsible for loading the generator with the demanded value and for measuring the produced power.

Reliable comparison between numerical investigations and the experiment requires obtaining the value of the internal power. This quantity is a result of thermodynamic processes in the turbine flow system and does not take into account the efficiency of the generator. The internal power can be directly computed in numerical analysis, but only the electrical power is measured in the experiment. Therefore, it is necessary to estimate the efficiency of the generator. The procedure of the estimation of the generator efficiency is described in details in Rusin *et al.* (2018b).

The roughness of the disc surface is of significant importance for the turbine performance. It may cause an increase of turbulence in the boundary layer and, therefore, an increase in shear stresses occurring on disc walls. In order to make CFD analysis more precise, it is recommended to determine this parameter. The roughness of the disc surface was measured with the use of Taylor-Hobson Surtronic 3+ Roughness Gage. Both sides of the rotor disc were surveyed. The measurement was carried out along 5 radii crossing outlet sections of the rotor and in two directions: parallel and normal with respect to the radius. The length of the measuring section totalled 0.8 mm. As a result, roughness expressed as the arithmetical mean deviation R_a was obtained. The value of R_a was calculated from the equation

$$R_a = \frac{1}{a} \sum_{i=1}^a |h_i| \quad (2.1)$$

where: h – roughness height, a – number of measurements.

The results obtained from experiments are presented in Section 5.

3. Numerical investigations

The numerical computations were conducted in ANSYS CFX software. The discretization was done using ANSYS Meshing tool and the setup of the numerical model was done in CFX. This software uses an implicit finite volume formulation to resolve discretized unsteady Reynolds-averaged Navier-Stokes equations. The calculations were carried out in steady and transient states in order to take account of unsteady phenomena, which may have an impact on turbine performance (e.g. Rulik *et al.*, 2015).

3.1. Geometrical model

Figure 2 presents the geometry model which was based on the geometrical features of the turbine prototype investigated previously in the experimental research.

The model consists of the supply system, rotor and the outlet system. In order to decrease computational cost as well as time, only half of the rotor was analysed. This configuration takes into account three inter-disc gaps; two of them are located between rotating discs and one between the turbine casing and the rotating disc. The diameter of the rotor discs was equal to 73 mm and the inter-discs gaps were 1.3 mm in thickness. The discs were separated by means of the spacers whose influence was also taken into consideration in the model. The rotor domain was supplied by the inlet system which consisted of a cylindrical chamber (1) with two inlet orifices with 1.8 mm in diameter (2) providing the working medium directly in between the discs. The chamber was 6 mm in diameter, 13 mm in length and was positioned at an angle 45° with respect

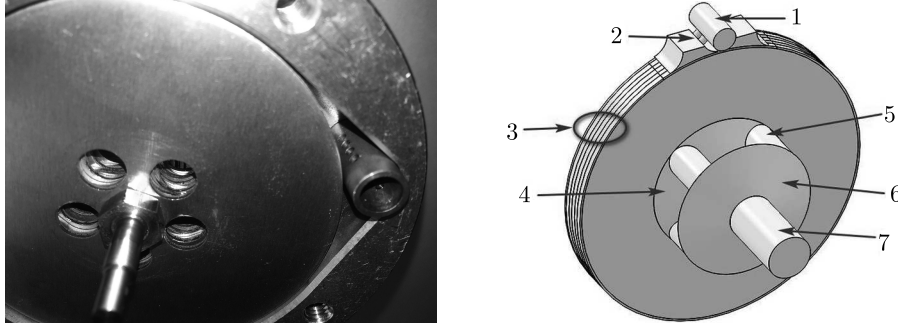


Fig. 2. Geometry of the numerical model

to the vertical symmetry axis of the rotor. Tip clearance (3) between the rotor and the casing was 0.5 mm in height. The outlet from the rotor consisted of 5 orifices with 7.5 mm in diameter, whose centres were located 10 mm away from the rotor axis. The working medium flowed out from the rotor to the converging collecting chamber (4) which was linked by four cylindrical ducts (5) with the second converging collecting chamber (6). Outflow into the ambient took place by means of 20 mm length duct (7) with 13 mm in diameter.

3.2. Numerical model and boundary conditions

Simulations were carried out for the air ideal gas. Conservation equations for mass, momentum and energy were solved

$$\begin{aligned} \frac{\partial \rho}{\partial t} + \frac{\partial}{\partial x_j}(\rho U_j) &= 0 \\ \frac{\partial \rho U_i}{\partial t} + \frac{\partial}{\partial x_j}(\rho U_i U_j) &= -\frac{\partial p}{\partial x_i} + \frac{\partial}{\partial x_j}(\tau_{ij} - \rho \overline{u_i u_j}) \\ \frac{\partial \rho h_{tot}}{\partial t} - \frac{\partial p}{\partial t} + \frac{\partial}{\partial x_j}(\rho U_j h_{tot}) &= \frac{\partial}{\partial x_j} \left(\lambda \frac{\partial T}{\partial x_j} - \rho \overline{u_j h} \right) + \frac{\partial}{\partial x_j} [U_j (\tau_{ij} - \rho \overline{u_i u_j})] \end{aligned} \quad (3.1)$$

where: ρ – density, p – pressure, h_{tot} – total enthalpy, x_i – coordinates in three directions, u_i – velocity in three directions, T – temperature, τ – stress tensor, λ – thermal conductivity. The high-resolution scheme was used to the discretized conservation equations in space. Integration with respect to time was done using the implicit second-order Euler scheme.

Laminar viscosity of the fluid changes with temperature, therefore the Sutherland formula (Sutherland, 1893) was applied in order to determine these changes

$$\mu(T) = \mu_{ref} \sqrt{\left(\frac{T}{T_{ref}}\right)^3 \frac{T_{ref} + T_S}{T + T_S}} \quad (3.2)$$

where: Sutherland temperature $T_S = 110.4$ K, reference viscosity $\mu_{ref} = 1.719 \cdot 10^{-5}$ Pa s, reference temperature $T_{ref} = 273.15$ K. The turbulence model used for simulations was $k-\omega$ SST (Menter, 1993), which is a combination of turbulence models: $k-\omega$ near the wall and $k-\varepsilon$ in the far field.

In most numerical software, the surface roughness is modelled by means of a downward shift function ΔB in the dimensionless velocity profile (Hama, 1954). It is based on the assumption of wall similarity (Flack and Schultz, 2014), which means that roughness does not change the shape of the mean velocity profile, so it is possible to determine a profile for smooth wall and then change its position (Fig. 3). It should be mentioned that this assumption does not have to be correct in some cases, especially for high values of roughness or the Reynolds number.

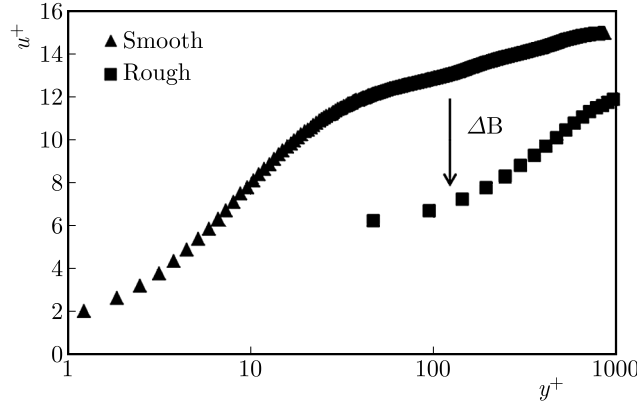


Fig. 3. The idea of the downward shift function ΔB

The dimensionless velocity profile and downward shift function are calculated using equations

$$u^+ = \frac{1}{\kappa} \ln(y^+) + B - \Delta B \quad \Delta B = \frac{1}{\kappa} \ln(1 + 0.3h_s^+) \quad h_s^+ = \frac{\varepsilon u_\tau}{\nu} \quad (3.3)$$

where κ – von Karman constant, h_s^+ – dimensionless sand grain roughness, ε – sand grain roughness, ν – kinematic viscosity. Sand grain roughness can be derived using arithmetical mean deviation of roughness height R_a (Adams *et al.*, 2012)

$$\varepsilon = \frac{2R_a}{\frac{\pi}{2} - \cos^{-1} \sqrt{1 - \frac{\pi^2}{16}} - \frac{\pi}{4} \sqrt{1 - \frac{\pi^2}{16}}} \quad (3.4)$$

This formula is based on the assumption that all protrusions are of spherical shape and equally distributed over the disc surface. Sand grain roughness was estimated with the use of results coming from experimental measurement. Additionally, in order to determine the influence of disc roughness on turbine performance, calculations for different values of roughness were conducted.

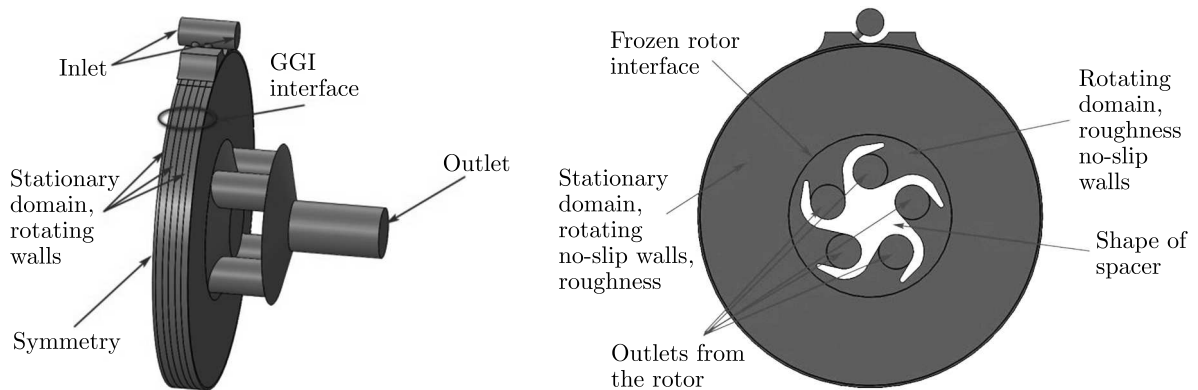


Fig. 4. Details of the numerical model

Figure 4 depicts the numerical model and boundary conditions. Inlet pressure equal to 3 bar or 4 bar and the total temperature equal to 303 K were applied at the inlet sections. The domain of the tip clearance was stationary, but its bottom wall adjacent to disc tips was rotating. The symmetry boundary condition was applied on one lateral wall of the tip clearance. The inter-disc gaps were stationary, but lateral walls were rotating. Additionally, sand grain roughness and no-slip wall were applied on these walls. Spacer domains were rotating and connected to the rotor with a frozen rotor interface. The outlet system was stationary and connected to the

spacer domain with the frozen rotor interface. Ambient pressure was applied at the outlet. All walls of the model were adiabatic.

Mesh independence study is presented in details in a paper by Rusin *et al.* (2018a). That study put emphasis on the boundary layer discretization as well as the time discretization. The final mesh consisted of approximately 5.1 M elements, and the time step was equal to 10^{-5} s.

4. Analytical model

The analytical model presented in this Section was developed by Guha and Sengupta (2013). Their motivation was to propose a three-dimensional analytical model describing velocity and pressure fields. The model makes use of the continuity (Eq. (4.1)₁), and momentum equations (Eqs. (4.1)_{2,3,4}) written for relative velocities in the cylindrical coordinates

$$\begin{aligned} \frac{\partial V_r}{\partial r} + \frac{V_r}{r} &= 0 & V_r \frac{\partial V_\theta}{\partial r} + \frac{V_\theta V_r}{r} + 2V_r \Omega &= \nu \frac{\partial^2 V_\theta}{\partial z^2} \\ V_r \frac{\partial V_r}{\partial r} - 2V_\theta \Omega - \Omega^2 r - \frac{V_\theta^2}{r} &= -\frac{1}{\rho} \frac{dp}{dr} + \nu \frac{\partial^2 V_r}{\partial z^2} & \frac{\partial p}{\partial z} &= 0 \end{aligned} \quad (4.1)$$

where: V – relative velocity, ν – kinematic viscosity, p – static pressure, Ω – rotational velocity, ρ – density, θ, r, z – circumferential, radial and axial directions. Boundary conditions assume that at the inlet to the rotor over the whole circumference there are constant averaged values of the circumferential and radial velocities. These values are changing in the inter-disc gaps in the axial direction according to the parabolic shape of the velocity profile. It is worth noting that this model skips the influence of the supply system and mutual interaction between the nozzles and the rotor. Additionally, the boundary layer is far from being fully developed at the upper part of the rotor, what is assumed in this model. It can have a significant impact on the prediction of the velocity gradient in the normal direction at the highest radius of the rotor and, hence, the tangential stresses and torque determination. Effects arising from the roughness of the discs were also not taken into account.

Integration of the r - and θ -momentum equations gives the set of following equations, which will make it possible to determine pressure and tangential velocity distribution along the radial direction

$$\begin{aligned} \frac{dp'}{dR} &= R + 2\zeta_m + \frac{6}{5} \frac{\zeta_m^2}{R} + \frac{6}{5} \frac{\varphi^2}{R^3} - 12 \frac{\nu \varphi}{\Omega b^2 R} \\ \frac{d\zeta_m}{dR} &= -\left(\frac{1}{R} + 10 \frac{\nu R}{\Omega \varphi b^2}\right) \zeta_m - \frac{10}{6} \\ \frac{d\zeta}{dR} &= -\left(\frac{1}{R} + 10 \frac{\nu R}{\Omega \varphi b^2}\right) \zeta - \frac{10}{6(\gamma - 1)} & \gamma &= \frac{\bar{U}_{\theta \text{ inlet}}}{\Omega r_{\text{inlet}}} \end{aligned} \quad (4.2)$$

where: $\varphi = V_{r \text{ inlet}}/(\Omega r_{\text{inlet}})$, $p' = (p - p_{\text{inlet}})/(\rho \Omega^2 r_{\text{inlet}}^2)$, $R = r/r_{\text{inlet}}$, b – length of inter-disc gap, $\bar{U}_{\theta \text{ inlet}}$ – average absolute circumferential velocity at the inlet to the rotor. Moreover, it is possible to estimate rotor power from the equation

$$N = \int_{r_{\text{outlet}}}^{r_{\text{inlet}}} \frac{6\mu\Omega r_{\text{inlet}}\zeta_m}{b} (2\pi r) r \, dr \quad (4.3)$$

5. Results

Results of experimental measurement of disc roughness are presented in Fig. 5. Distribution of the roughness is not uniform in all directions and varies within 0.16 and 0.40. Average roughness

totals $R_a = 0.28 \mu\text{m}$, which proves that the surface is of high quality. Figure 6 depicts the influence of disc roughness on power prediction for inlet pressure 3 bar and rotational velocity $n = 25000 \text{ min}^{-1}$. It can be seen that even a small increase in the roughness can lead to a visible rise in power prediction, although this effect gets smaller as the roughness increases.

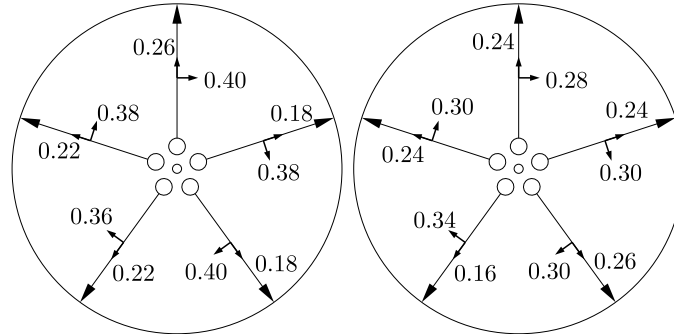


Fig. 5. Roughness of the disc surface

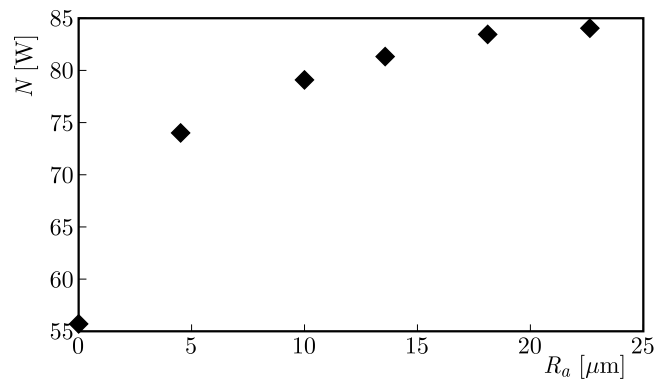


Fig. 6. The influence of roughness on power

Between a smooth disc and $R_a = 4.5$, there is an almost 35% (20 W) rise in the generated power. Between $R_a = 10$ and $R_a = 23$, the difference in the power is only 5 W. This improvement can be explained with the analysis of the flow regime on the disc surface area, which is presented in Fig. 7. The flow regime is defined according to the dimensionless sand grain roughness h_s^+ formula (Schlichting, 1979). For $h_s^+ < 5$, the flow is considered to be hydraulically smooth. In such a case, all protrusions are covered by a viscous sublayer and eddies created by the roughness can be damped by viscosity. For $5 < h_s^+ < 70$, the flow is in a transition regime. Some of the protrusions are extended above the viscous sublayer, therefore, the disturbances can not be damped by viscosity and they have an impact on the momentum diffusion. For $h_s^+ > 70$, the flow is rough and the viscous effects become negligible. It can be seen in Fig. 7 that the area with the jet is characterised by a highly rough regime, but as the fluid velocity decreases, the flow become transitional. Most of the flow is in this regime, and some areas are even in the smooth regime, especially near the outflow from the rotor. The wall shear stress increases due to the rise in eddy viscosity, which also influences the power. Distribution of the unit power for roughness $R_a = 0.28$ and $R_a = 23$ is presented in Fig. 8. The shape of contours is similar in both cases, but values are much higher for the bigger roughness. Maximum values of the unit power occur in the jet and are equal to approximately 65000 W/m^2 for $R_a = 0.28$ and 100000 W/m^2 for $R_a = 23$. The jet is responsible for 25.5% and 40.8% of the generated power for those cases respectively. It is also worth noting that in both cases there are areas with a negative unit power. These areas occur between the jet and disc tip and at the inlet to the rotor. In both cases the

negative power is caused by specific flow field structures: swirls, vortices and rapid changes in velocities. Moreover, there is an interaction between disc tips and the lateral flow, which takes place in the tip clearance.

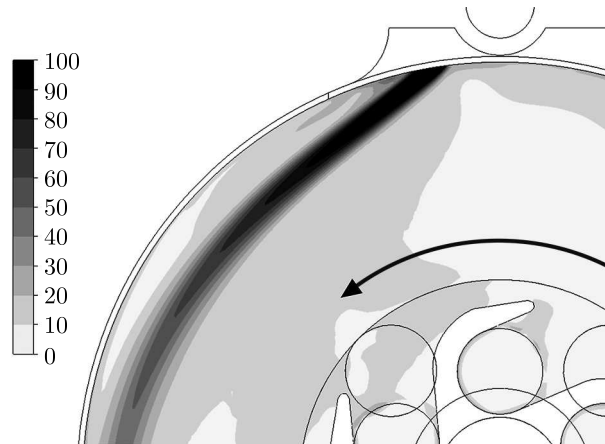


Fig. 7. Flow regime h_s^+ on the disc surface for $R_a = 4.5$

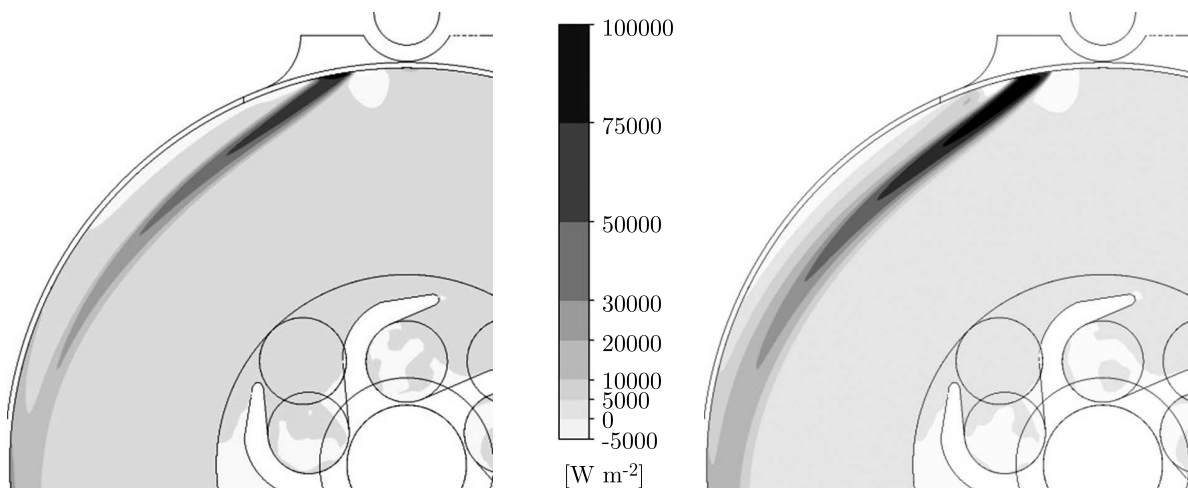


Fig. 8. Unit power distribution for roughness $R_a = 0.28$ (left) and $R_a = 23$ (right)

Figures 9a and 9b depict power and efficiency characteristics for inlet pressure equal to 3 bar and 4 bar in the experiment and numerical analysis (CFD), respectively. Maximum values are: 55.6 W (25000 min^{-1}) for 3 bar CFD, 42.5 W (20500 min^{-1}) for 3 bar experiment, 98.3 W (30000 min^{-1}) for 4 bar CFD and 71.5 W (22500 min^{-1}) for 4 bar experiment.

All characteristics are parabolic and relatively flat, which means that in a wide range of rotational velocity the power changes insignificantly, e.g. for 3 bar the CFD power varies only 25% of the maximum value. Values obtained from numerical investigations are higher than values obtained from the experiment.

The efficiency was computed from the formula

$$\eta = \frac{N}{\dot{m}T_{in}c_p \left(1 - \left(\frac{p_{out}}{p_{in}} \right)^{\frac{\kappa-1}{\kappa}} \right)} \quad (5.1)$$

where: \dot{m} – mass flow, T_{in} – inlet temperature, c_p – specific heat capacity at constant pressure, p_{in} , p_{out} – pressure at inlet and outlet, κ – heat capacity ratio. Maximum efficiency values

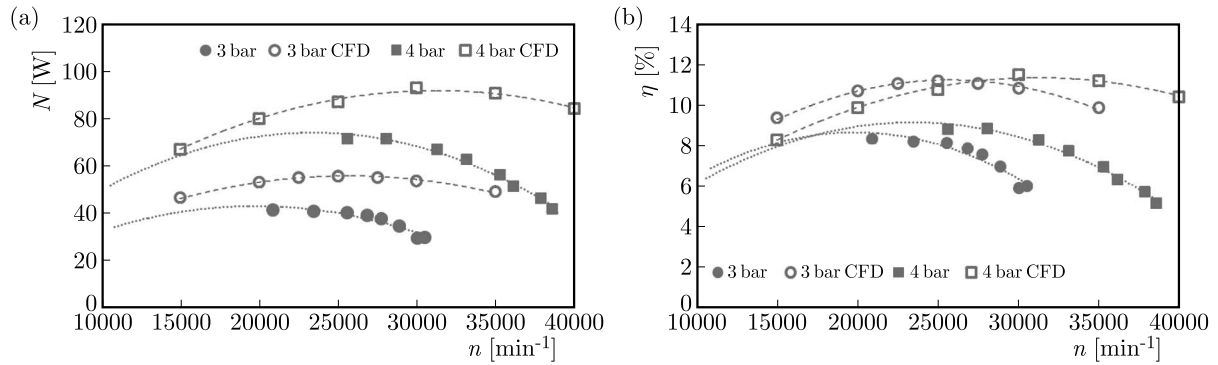


Fig. 9. Characteristics of (a) power and (b) efficiency versus rotational velocity

correspond to the maximum power and are equal to: 11.2% for 3 bar CFD, 8.4% for 3 bar experiment, 11.8% for 4 bar CFD and 8.9% for 4 bar experiment. An increase of inlet pressure causes a shift of the maximum efficiency toward higher rotational velocities.

The differences between the experiment and simulations were caused by flaws in both the numerical model and set up of the test stand. The main issue in the experiment was a mediocre precision of turbine manufacturing and leakages in the inlet system. The characteristic of the generator efficiency was determined only for a limited range and the uncertainty of the generator efficiency for higher rotational velocity increases. It can be seen that, the higher rotational velocity, the bigger differences between results obtained from CFD and experiment.

The numerical model has its own flaws as well. The biggest challenge comes from flow rotation. An additional body force occurs and it interacts with turbulence (Tucker, 2013). This may lead to a false prediction of eddy viscosity and, thereby, the power. The use of a rotation-curvature correction suggested by Spalart and Shur (1997), and implemented into the SST model by Smirnov and Menter (2009), in our case did not change the power prediction.

RANS method also tends to underpredicts turbulence mixing in developing jets, so it overpredicts the momentum which causes a larger effect on the rotational velocity of the disc, thus power, with respect to reality.

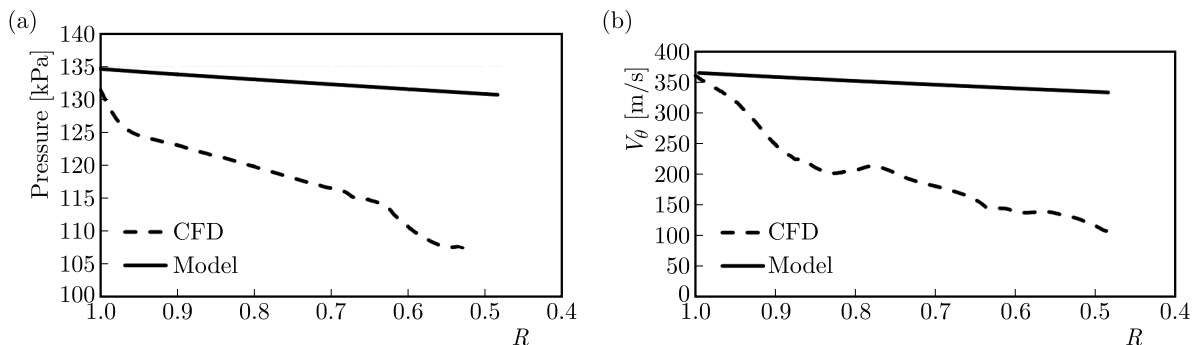


Fig. 10. Radial distribution of (a) pressure and (b) circumferential velocity for numerical analysis and the analytical model for gap 2

Results obtained from the analytical model are presented in this Section. Figures 10a and 10b present the radial distribution of pressure and circumferential velocity as a function of non-dimensional radius R . The value of $R = 1$ corresponds to the rotor inlet and $R = 0.48$ corresponds to the rotor outlet. Assumptions used for the analytical model require the use of the averaged values of circumferential velocity and radial velocity at the inlet to the rotor in the calculations. However, it is impossible to determine reliable values of these quantities due to specific supply geometry (one supply nozzle over each of the inter-disc gap instead of a uniform

supplying over the whole circumference of the rotor as assumed in the model). For this reason, path lines of the fluid particles from the point where the jet enters the rotor were determined (Fig. 11a), and the value of circumferential velocity at the beginning of the streamline was used in the analytical calculations. Radial velocity was calculated with the use of the continuity equation at the inlet to the rotor for each of the inter-disc gaps. It is worth noting that this velocity component differs substantially for each inter-disc gap (up to an order of magnitude). It means that most of the mass flow rate flows through gap 1. In this part, one surface of the disc is rotating, but the second wall of this gap belongs to the turbine casing, hence, it is stationary. The centrifugal force coming from rotational velocity is weaker compared to other gaps and the fluid follow that way due to the lowest resistance. This effect is partially visible in Fig. 11b, which depicts velocity vectors. A part of the working medium is flowing into gap 1 immediately after outflowing from the nozzles.

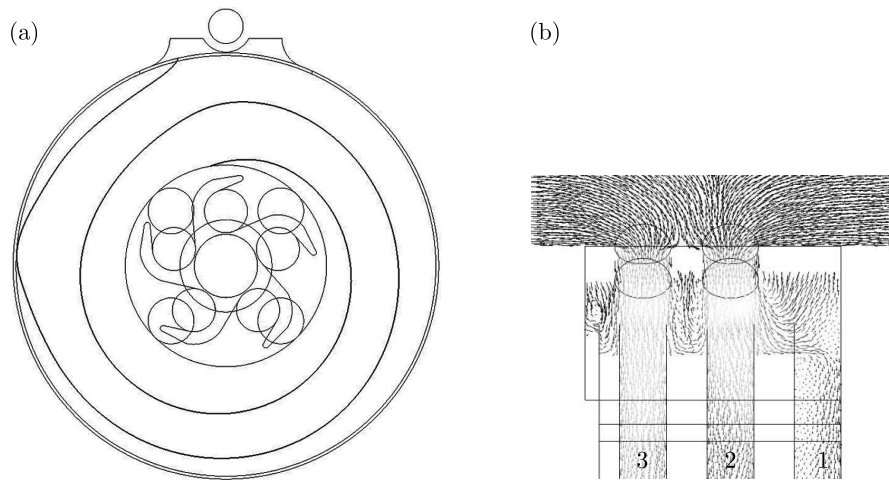


Fig. 11. (a) Example of a streamline. (b) Velocity vectors on the cross-section of the nozzles

Distributions of circumferential velocity and pressure along the streamlines were compared to the results obtained from the analytical model. It is visible in Figs. 10a and 10b that there are significant differences between the results obtained from numerical simulations (CFD) and the analytical model (Model). Pressure is linearly decreasing from the starting value of 134.5 kPa up to 130.5 kPa. In the case of the CFD, a pressure drop is linear only in the middle section of the gap. The inlet and outlet from the rotor are characterized by disturbances or flow phenomena like overexpansion, hence, there are more rapid changes. Expansion ends at the value of 107 kPa. The authors of the analytical model suggested iteratively changing the value of Ω in order to obtain the assumed pressure drop. However, in the investigated case, the rotational velocity was set in the numerical model and it seems unjustified to change it. A similar situation occurs for the circumferential velocity distribution. The analytical model predicted a linear drop from 365 m/s to 330 m/s while CFD calculations gave a drop from 365 m/s to 100 m/s. Figure 12 presents a comparison of the power obtained from the analytical model and from the numerical analysis for each inter-disc gap (labelled as in Fig. 11b) and the total power output for 3 bar and 4 bar and 30000 min^{-1} . Due to the fact that there are different flow conditions at the inlet to the rotor, the power was separately calculated according to Eq. (4.3) for each inter-disc gap. For clarity, the power was also multiplied by factor 2 to make it possible to compare the results with the experimental investigations. It can be seen that the power obtained from gaps 2 and 3 are almost equal for both cases of CFD while the differences for these regions are big in the analytical model.

It is also worth noting that the analytical model predicts a negative power from gap 1 while CFD simulation proves a positive contribution from this region. Comparison between the

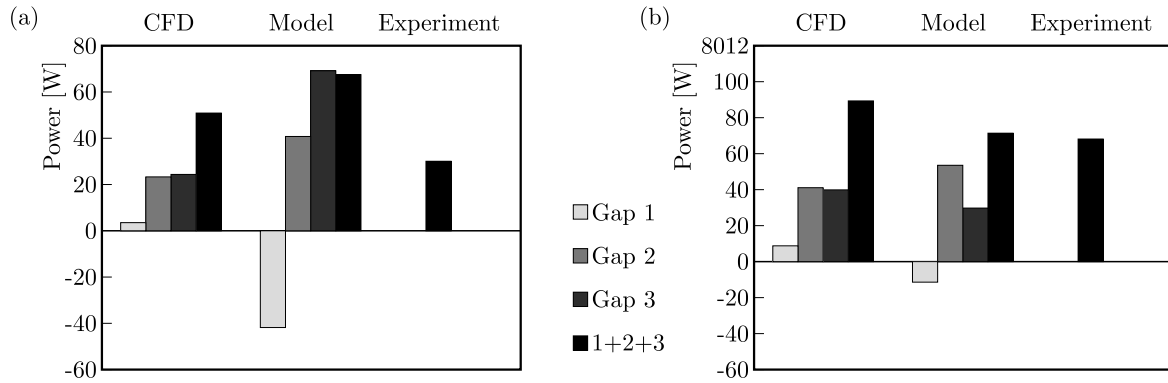


Fig. 12. Comparison of the power obtained from inter-disc gaps in CFD, the analytical model and experiment for 30000 min^{-1} and inlet pressure 3 bar (left) and 4 bar (right)

methods shows that the analytical model is closer to the experiment in the case of 4 bar but highly deviates from the experiment in the case of 3 bar. This could be elucidated by the problem of determining the correct values of radial and circumferential velocities for the analytical model. High tip flows complicate determination of appropriate values for each gap. A part of the fluid in the jet can switch into other gaps once it reaches the tip clearance (partially visible in Fig. 11a on the left side of the streamline). Therefore, determination of the radial velocity component based on the mass flow in the inter-disc entrance can give unreliable values. CFD analysis overestimates the power value in each case.

6. Conclusions

Numerical and experimental investigations of a prototype model of Tesla turbine is presented in the paper. It was possible to measure the power and efficiency characteristics for inlet pressure of 3 bar and 4 bar. Maximum obtained power values were equal to 42.5 W and 71.5 W with the corresponding efficiency 8.4% and 8.9%. Roughness measurement of one of the rotor disc totalled $R_a = 0.28$, which indicated on the polished surface. Numerical investigations were carried out basing on test stand conditions. The obtained power and efficiency was overestimated with a comparison to experiment. The highest power and efficiency values were: 55.6 W, 11.2% for inlet pressure 3 bar and 98.3 W, 11.8% for 4 bar. Parameter distributions from the numerical analysis were used as boundary conditions in the analytical model. Distributions of pressure and circumferential velocity in the radial direction were underestimated by the analytical model in comparison to CFD. The inter-disc gap between the rotor and turbine casing contributes to low values of power and efficiency as there is small resistance, and the working medium is sucked without expanding in the rotor. It is recommended to limit the flow in that direction as much as possible.

The visible discrepancy between results obtained from different models proves that in Tesla turbine investigation many factors can contribute to physical aspects of the energy transfer between the flow and the generator output, and it is necessary to improve the model details as well as the precision of measurements. CFD modelling with RANS approach can give information about global properties of the flow in Tesla turbine, but more details can be obtained only with more advanced methods, e.g. Large Eddy Simulation.

Acknowledgements

The presented work was performed within the Silesian University of Technology statutory research funds for young scientists. This research was partially supported by the PL-Grid Infrastructure.

References

1. ADAMS T., GRANT C., WATSON H., 2012, A simple algorithm to relate measured surface roughness to equivalent sand-grain roughness, *International Journal of Mechanical Engineering and Mechatronics*, **1**, 1, 66-71
2. BARBARELLI S., FLORIO G., SCORNAIENCHI N.M., 2018, Developing of a small power turbine recovering energy from low enthalpy steams or waste gases: Design, building and experimental measurements, *Thermal Science and Engineering Progress*, **6**, 346-354
3. BOCHON K., CHMIELNIAK T., 2015, Energy and economic analysis of the carbon dioxide capture installation with the use of monoethanolamine and ammonia, *Archives of Thermodynamics*, **36**, 1, 93-110
4. BORATE H.P., MISAL N.D., 2012, An effect of spacing and surface finish on the performance of bladeless turbine, *ASME 2012 Gas Turbine India Conference, GTINDIA 2012*, 165-171
5. CAREY V.P., 2010, Assessment of Tesla turbine performance for small scale Rankine combined heat and power systems, *Journal of Engineering for Gas Turbines and Power*, **132**, 122301-1-122301-8
6. DENG Q., QI W., FENG Z., 2013, Improvement of a theoretical analysis method for Tesla turbines, *ASME Turbo Expo 2013: Turbine Technical Conference and Exposition, GT 2013*, San Antonio, United States
7. DYKAS S., MAJKUT M., SMOLKA K., STROZIK M., 2015, Experimental research on wet steam flow with shock wave, *Experimental Heat Transfer*, **28**, 5, 417-429
8. FLACK K.A., SCHULTZ M.P., 2014, Roughness effects on wall-bounded turbulent flows, *Physics of Fluids*, **26**, 101305-1-101305-17
9. FRĄCZEK D., WRÓBLEWSKI W., BOCHON K., 2017, Influence of honeycomb rubbing on the labyrinth seal performance, *Journal of Engineering for Gas Turbines and Power*, **139**, 1, 012502
10. GUHA A., SENGUPTA S., 2013, The fluid dynamics of the rotating flow in a Tesla disc turbine, *European Journal of Mechanics B/Fluids*, **37**, 112-123
11. HAMA F.R., 1954, Boundary-layer characteristics for rough and smooth surface, *Transactions of the SNAME*, **62**, 333-351
12. LI R., WANG H., YAO E., LI M., NAN W., 2017, Experimental study on bladeless turbine using incompressible working medium, *Advances in Mechanical Engineering*, **9**, 1, 1-12
13. LAMPART P., JĘDRZEJEWSKI Ł., 2011, Investigations of aerodynamics of Tesla bladeless turbine, *Journal of Theoretical and Applied Mechanics*, **49**, 2, 477-499
14. LAMPART P., KOSOWSKI K., PIWOWARSKI M., JĘDRZEJEWSKI Ł., 2009, Design analysis of Tesla micro-turbine operating on a low-boiling medium, *Polish Maritime Research*, **63**, 16, 28-33
15. MENTER F., 1993, Zonal two equation $k-\omega$ turbulence models for aerodynamic flows, *24th Fluid Dynamics Conference*, Orlando, USA
16. NECKEL A.L., GODINHO M., 2015, Influence of geometry on the efficiency of convergent – divergent nozzles applied to Tesla turbines, *Experimental Thermal and Fluid Science*, **62**, 131-140
17. RULIK S., WRÓBLEWSKI W., NOWAK G., SZWEDOWICZ J., 2015, Heat transfer intensification using acoustic waves in a cavity, *Energy*, **87**, 1, 21-30
18. RUSIN K., WRÓBLEWSKI W., RULIK S., 2018a, The evaluation of numerical methods for determining the efficiency of Tesla turbine operation, *Journal of Mechanical Science and Technology*, **32**, 12, 5711-5721
19. RUSIN K., WRÓBLEWSKI W., STROZIK M., 2018b, Experimental and numerical investigations of Tesla turbine, *Journal of Physics: Conference Series*, **1101**, 1, 012029
20. SCHLICHTING H., 1979, *Boundary Layer Theory*, McGraw-Hill Book Company, New York

21. SCHOSSER C., FUCHS T., HAIN R., LECHELER S., KÄHLER CH., 2016, Three-dimensional particle tracking velocimetry in a Tesla turbine rotor using non-intrusive calibration method, *18th International Symposium on the Application of Laser and Imaging Techniques to Fluid Mechanics*, Lisbon, Portugal
22. SENGUPTA S., GUHA A., 2012, A theory of Tesla disc turbines, *Journal of Power and Energy*, **226**, 650-663
23. SMIRNOV P.E., MENTER F.R., 2009, Sensitization of the SST turbulence model to rotation and curvature by applying the Spalart-Shur correction term, *Journal of Turbomachinery*, **131**, 4, 2305-2314
24. SONG J., REN X., LI X., GU C., ZHANG M., 2018, One-dimensional model analysis and performance assessment of Tesla turbine, *Applied Thermal Engineering*, **134**, 546-554
25. SPALART P.R., SHUR M.L., 1997 On the sensitization of turbulence models to rotation and curvature, *Aerospace Science and Technology*, **1**, 5, 297-302
26. SUTHERLAND W., 1893, The viscosity of gases and molecular force, *Philosophical Magazine*, **5**, 36, 507-531
27. SZABLOWSKI Ł., KRAWCZYK P., BADYDA K., KARELLAS S., KAKARAS E., BUJALSKI W., 2017, Energy and exergy analysis of adiabatic compressed air Energy storage system, *Energy*, **138**, 12-18
28. Tesla N., Turbine, Patent No: 1,061,206, United States Patent Office of New York, 1913
29. TUCKER P.G., 2013, Trends in turbomachinery turbulence treatments, *Progress in Aerospace Sciences*, **63**, 1-32
30. WRÓBLEWSKI W., FRĄCZEK D., MARUGI K., 2018, Leakage reduction by optimisation of the straight-through labyrinth seal with a honeycomb and alternative land configurations, *International Journal of Heat and Mass Transfer*, **126**, 725-739

Manuscript received December 21, 2018; accepted for print February 7, 2019